Extreme many-body scarring in a quantum spin chain via weak dynamical constraints

Shane Dooley [1,2,*] and Graham Kells[2,3,†]

[1]*Department of Physics, Trinity College Dublin, Dublin 2, Ireland*
[2]*School of Theoretical Physics, Dublin Institute for Advanced Studies, 10 Burlington Rd, Dublin 4, Ireland*
[3]*School of Physical Sciences, Dublin City University, Glasnevin, Dublin 9, Ireland*

It has recently been established that quantum many-body scarring can prevent the thermalization of some isolated quantum systems starting from certain initial states. One of the first models to show this was the so-called PXP Hamiltonian, which was used to theoretically model an experiment on a chain of strongly interacting Rydberg atoms. A defining feature of the PXP Hamiltonian is a set of dynamical constraints that make certain states inaccessible to the dynamics. In this paper we construct a class of spin chain models that are parameterized by a discrete variable ℓ that controls the "strength" of a dynamical constraint. We show that by increasing ℓ the constraint becomes weaker in the sense that fewer states are excluded from the dynamics. The PXP Hamiltonian is a special case for $\ell = 2$. By weakening the constraint to $\ell \geqslant 4$, however, we find a more extreme version of quantum scarring than in the PXP Hamiltonian with the number of scar states growing exponentially in the system size.

I. INTRODUCTION

A hot cup of tea, left on the counter, will eventually cool to room temperature, losing all information encoded in its initial conditions. A similar process of thermalization is also expected in generic isolated quantum systems. At present, this is best understood through the eigenstate thermalization hypothesis (ETH) [1], which conjectures that an isolated quantum system themalizes because its individual energy eigenstates $|E\rangle$ appear thermal with respect to expectation values of realistic observables $\hat{\mathcal{O}}$ (that is, $\langle E|\hat{\mathcal{O}}|E\rangle \approx \mathcal{O}_{\text{th}}(E)$ where $\mathcal{O}_{\text{th}}(E)$ is the thermal expectation value at the energy E).

It is well established that some systems can fail to thermalize. Integrable models, for example, have a large number of local integrals-of-motion that constrain the dynamics so that the state space cannot be explored ergodically. From the perspective of the ETH, this failure to thermalize in quantum integrable models is attributed to rare nonthermal, i.e., $\langle E|\hat{\mathcal{O}}|E\rangle \not\approx \mathcal{O}_{\text{th}}(E)$, energy eigenstates $|E\rangle$ of its Hamiltonian [2]. Similar behavior is also expected in many-body localized (MBL) models, where disorder-induced local integrals-of-motion lead to an effective integrability [3–5].

For nonintegrable systems, anomalous thermalization can arise, for example, via pre-thermalization [6–8], strong zero modes [9–11], or metastability [12,13]. Recently, however, it was also discovered that some nonintegrable systems can fail to thermalize due to rare nonthermal eigenstates called quantum many-body scars (QMBS) [14–30]. One of the first and most prominent examples of QMBS is in the so-called PXP Hamiltonian [23–27], which was used to model an experiment on a chain of interacting Rydberg atoms [31,32]. A defining feature of the PXP Hamiltonian is a constraint that makes certain states inaccessible to the dynamics. Similar dynamical constraints also play a central role in a systematic route to constructing QMBS via the "embedding method" of Ref. [14] and in the anomalously slow thermalization observed in Refs. [12,13].

In this paper, our aim is to further explore the role of such local dynamical constraints in ETH-violation. To this end, in Section II we construct a family of spin chain models that generalizes the PXP model. The key feature here is a discrete variable ℓ that controls the strength of a dynamical constraint. For the strongest nontrivial constraint ($\ell = 2$) we recover the PXP Hamiltonian. Increasing ℓ weakens the constraint in the sense that fewer states are excluded from the dynamics.

In Section III, we show that the scarring (i.e., the number of nonthermal states) becomes more extreme when the constraint is weakened. This is directly observable in the behavior of the eigenstate expectation values (EEVs) $\langle E|\hat{\mathcal{O}}|E\rangle$ and in their fluctuations around their microcanonical average. We argue that this behavior occurs because, as ℓ increases, the number of energy eigenstates $|E\rangle$ that can evade the constraint grows dramatically. On the other hand, for finite ℓ, it remains the case that most eigenstates $|E\rangle$ do not evade the constraint. Thus the generic behavior of the bulk spectrum remains distinctly thermal.

II. MODEL

We consider a one-dimensional chain of L spin-1/2 particles with the Hamiltonian

$$\hat{H}_\ell = \hat{P}_\ell \hat{H}_0 \hat{P}_\ell, \quad \hat{H}_0 = \frac{\Omega}{2} \sum_{i=1}^{L} \hat{\sigma}_i^x, \quad (1)$$

*dooleysh@gmail.com
†gkells@stp.dias.ie

where the projector,

$$\hat{P}_\ell = \prod_i (\hat{\mathbb{1}} - |\uparrow_i \uparrow_{i+1} \ldots \uparrow_{i+\ell-1}\rangle\langle\uparrow_i \uparrow_{i+1} \ldots \uparrow_{i+\ell-1}|), \quad (2)$$

enforces a dynamical constraint of radius $\ell \in \{1, 2, ..., L\}$. Here $\{|\uparrow_i\rangle, |\downarrow_i\rangle\}$ is a basis for the spin-1/2 subsystem at site i of the chain and $\hat{\sigma}_i^x = |\uparrow_i\rangle\langle\downarrow_i| + |\downarrow_i\rangle\langle\uparrow_i|$.

The constraint can be seen as excluding any states with ℓ consecutive $\uparrow$ states from the dynamics, giving a constrained state space that is smaller than the full 2^L-dimensional unconstrained state space. For example, if $\ell = 3$, states such as $|\ldots \uparrow\uparrow\uparrow \ldots\rangle$ are annihilated by the projector $\hat{P}_{\ell=3}$ and are, therefore, trivial zero-energy eigenstates of the Hamiltonian $\hat{H}_{\ell=3}$ and may be neglected. The PXP Hamiltonian is a special case for $\ell = 2$.

In Appendix A we show that our Hamiltonian Eq. (1) may be derived as an effective model, starting from an underlying Hamiltonian with strong ℓ-body interactions between the spin-1/2 particles on the chain. Since ℓ-body interactions may be considered unphysical for large ℓ we also show in Appendix A that our Hamiltonian can be mapped to a more physically plausible underlying model with two-body interactions between higher-spin particles. We also note that the constraints in our Hamiltonian Eq. (1) can, in principle, be generated by repeated fast projective measurements, as was done experimentally in Ref. [33] for $\ell = L$.

Our constrained Hamiltonian $\hat{H}_\ell$ has several symmetries. A reflection $i \to L - i + 1$ of site indices about the midpoint of the chain leaves the Hamiltonian invariant, implying that it has a spatial parity symmetry. Also, if there are periodic boundary conditions (PBC), the Hamiltonian has a translation symmetry under the transformation $i \to i + 1$ of the site index. In the following, we can restrict to a symmetry sector of $\hat{H}_\ell$ to reduce the numerical cost of calculating its eigensystem.

III. RESULTS

A. Increasing ℓ weakens the dynamical constraint

Let $\mathcal{D}_{L,\ell}$ denote the dimension of the constrained state space of the Hamiltonian $\hat{H}_\ell$ in a chain of length L. The strongest possible constraint is for $\ell = 1$ since the constrained Hilbert space dimension is $\mathcal{D}_{L,1} = 1$ and only the state $|\downarrow\rangle^{\otimes L}$ is allowed. The constraint becomes weaker as ℓ increases in the sense that fewer and fewer states are excluded from the constrained state space. The weakest possible constraint is for $\ell = L$, since only a single state $|\uparrow\rangle^{\otimes L}$ is excluded and the constrained state space dimension is $\mathcal{D}_{L,L} = 2^L - 1$.

More generally, for a spin chain with open boundary conditions (OBC) the dimension $\mathcal{D}_{L,\ell}^{\text{OBC}}$ of the constrained subspace is given by the recurrence relation (see Appendix B for the proof)

$$\mathcal{D}_{L,\ell}^{\text{OBC}} = \mathcal{D}_{L-1,\ell}^{\text{OBC}} + \mathcal{D}_{L-2,\ell}^{\text{OBC}} + \ldots + \mathcal{D}_{L-\ell,\ell}^{\text{OBC}} \quad (3)$$

with the initial conditions $\mathcal{D}_{L,L}^{\text{OBC}} = 2^L - 1$ and $\mathcal{D}_{L,\ell}^{\text{OBC}} = 2^L$ if $L < \ell$. This recurrence relation defines a generalized Fibonacci sequence in which the next number in the sequence is obtained as the sum of the previous ℓ numbers. For instance, $\mathcal{D}_{L,2}^{\text{OBC}}$ is the $(L + 2)$-th number in the usual Fibonacci
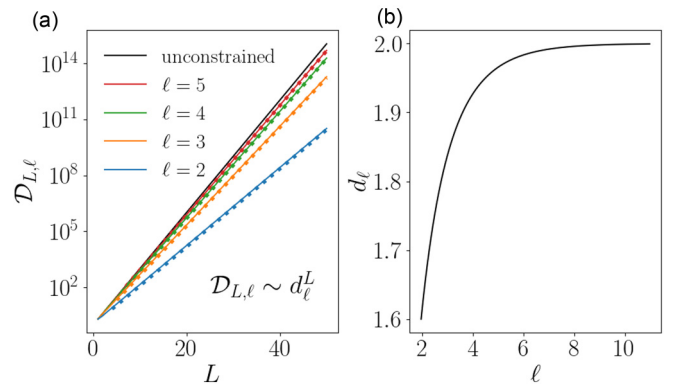

FIG. 1. (a) For $L \gg 1$ the constrained state space dimension increases exponentially in the system size $\mathcal{D}_{L,\ell} \sim (d_\ell)^L$ (solid lines for OBC and dotted lines for PBC are almost indistinguishable in the figure). For OBC one can show that d_ℓ is the solution to the equation $\ell = \log(2 - d_\ell)^{-1} / \log d_\ell$, which is plotted in (b) (see Ref. [35], p. 101). For $\ell = 2$ this gives $d = (1 + \sqrt{5})/2$, the golden ratio, while for $\ell \to \infty$ we have $d \to 2$.

sequence [23,34], while $\mathcal{D}_{L,3}^{\text{OBC}}$ is the $(L + 3)$-th number in the so-called tribonacci sequence.

For PBC, the constrained Hilbert space dimension has the slightly more complicated form (again, see Appendix B for the proof)

$$\mathcal{D}_{L,\ell}^{\text{PBC}} = \mathcal{D}_{L-1,\ell}^{\text{OBC}} + \mathcal{D}_{L-3,\ell}^{\text{OBC}} + 2\mathcal{D}_{L-4,\ell}^{\text{OBC}}$$
$$+ 3\mathcal{D}_{L-5,\ell}^{\text{OBC}} + \ldots + (\ell - 1)\mathcal{D}_{L-\ell-1,\ell}^{\text{OBC}}. \quad (4)$$

In Fig. 1(a) we plot $\mathcal{D}_{L,\ell}$ as a function of the system size L for both OBC and PBC. We see that for $L \gg 1$ the constrained state space dimension grows exponentially in the system size $\mathcal{D}_{L,\ell} \sim d_\ell^L$ for some number d_ℓ. Figure 1(b) shows d_ℓ as a function of the constraint radius ℓ. As ℓ increases, d_ℓ also increases with $d_\ell \to 2$ in the $\ell \to \infty$ limit. We interpret this as meaning that increasing ℓ weakens the dynamical constraint, and that the constraint becomes negligible as $\ell \to \infty$.

B. The finite-ℓ constraint breaks integrability

The unconstrained Hamiltonian $\hat{H}_0 = \frac{\Omega}{2} \sum_i \hat{\sigma}_i^x$ is noninteracting and is clearly integrable. However, the constraint $\hat{P}_\ell$ breaks the integrability for finite ℓ. This is shown numerically in the left column of Fig. 2 where we plot the normalized level spacing distribution $p(s_\alpha/\bar{s})$, where $s_\alpha = E_{\alpha+1} - E_\alpha$ is the spacing between two consecutive energy eigenvalues in a narrow energy window, and $\bar{s}$ is the mean level spacing in the energy window. We note that in calculating $p(s_\alpha/\bar{s})$ we restrict to the even-reflection and zero-momentum (we have assumed PBC) symmetry sector of $\hat{H}_\ell$. For $\ell \in \{2, 3, \ldots, 6\}$ the distribution shows clear level-repulsion and is close to the distribution of the Gaussian orthogonal ensemble (GOE) of random matrices, as expected for a nonintegrable Hamiltonian.

Another standard numerical test of integrability is to compute the r value [36], defined as $\langle r_\alpha \rangle = \langle \min(s_\alpha, s_{\alpha+1}) / \max(s_\alpha, s_{\alpha+1}) \rangle$, where the average $\langle \bullet \rangle$ is taken over all eigenvalues in the symmetry sector. In Fig. 3 we see that a slightly perturbed (see caption to Fig. 3) $\hat{H}_0$
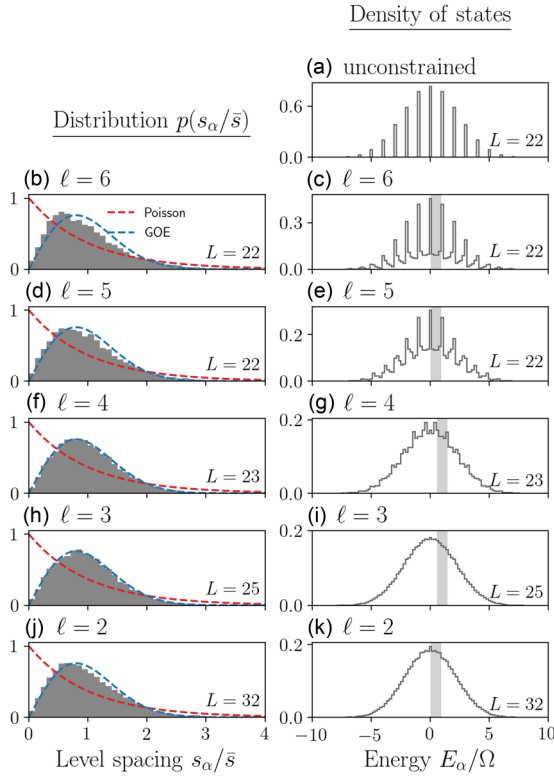
FIG. 2. Left column: The distribution of energy level spacings $p(s_\alpha/\bar{s})$ in the zero-momentum and even reflection-parity symmetry sector of $\hat{H}_\ell$. Level statistics are calculated in an energy window $\Lambda_E = [E - \Delta E, E + \Delta E]$, shown in the gray shaded region in the corresponding figure in the right column. The energy window Λ_E is chosen so that it excludes the degenerate peaks (when $\ell \geqslant 4$), but captures the states between two peaks. This is achieved for an energy window with $\Delta E = 0.45\Omega$, centered at $E = 0.5\Omega$ if L is even or $E = \Omega$ if L is odd. Right column: The density of states of $\hat{H}_\ell$ in its zero-momentum and even reflection-parity symmetry sector. The sharp peaks correspond to degeneracies in the spectrum.

is integrable, but that the constraint $\hat{H}_\ell = \hat{P}_\ell \hat{H}_0 \hat{P}_\ell$ breaks the integrability for $\ell \in \{2, 3, \ldots, 7\}$. In fact, Fig. 3 shows that the integrability is broken more strongly for $\ell \geqslant 3$ than for the PXP model ($\ell = 2$) in the sense that the r value approaches the GOE value more quickly as the symmetry sector dimension increases.

C. Degeneracies in the $\ell \geqslant 4$ constrained Hamiltonian

The eigenstates of the unconstrained Hamiltonian $\hat{H}_0 = \frac{\Omega}{2}\sum_i \hat{\sigma}_i^x$ are the product states $\{|x_1, x_2, \ldots, x_L\rangle\}$, where each $|x_i\rangle \in \{|\pm\rangle\}$ is a $\hat{\sigma}^x$ eigenstate. The eigenvalues $E_\alpha = \frac{\Omega}{2}\sum_{i=1}^L x_i$ are highly degenerate and are integer multiples of Ω (for even L) or half integer multiples of Ω (for odd L). This is illustrated in Fig. 2(a), where a histogram shows the density of states in the zero-momentum, even-reflection symmetry sector. The degeneracies are indicated in the histogram by sharp peaks at integer/half integer multiples of Ω. Of course, any linear combination of degenerate eigenstates is also a valid eigenstate. For example, the Dicke states $|j, m_x\rangle$, defined as simultaneous eigenstates of $\hat{J}^x \equiv \frac{1}{2}\sum_{j=1}^L \hat{\sigma}_j^x$ (with eigen-
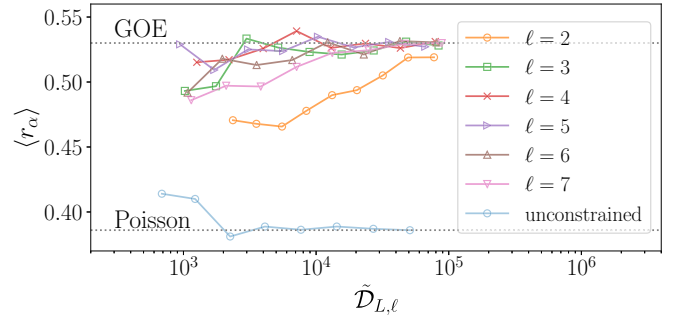

FIG. 3. The r value is a standard numerical test of integrability. Here we plot the plot the r value as a function of the dimension $\tilde{\mathcal{D}}_{L,\ell}$ of the zero-momentum, even-reflection symmetry sector of $\hat{H}_\ell = \hat{P}_\ell \hat{H}_0 \hat{P}_\ell$. For the unconstrained model we have $\langle r_\alpha \rangle \to 0.386$ as the system size increases, as expected for an integrable model. For $\ell \geqslant 2$, however, it tends toward the value $\langle r_\alpha \rangle \approx 0.53$ that is expected for nonintegrable systems (GOE). [Note that we have used a slightly perturbed unconstrained Hamiltonian, $\hat{H}_0 = \frac{\Omega}{2}\sum_{i=1}^L \hat{\sigma}_i^x + \lambda \sum_i (\hat{\sigma}_i^x \hat{\sigma}_{i+1}^z + \hat{\sigma}_i^z \hat{\sigma}_{i+1}^x)$, with $\lambda = 0.01 \times \Omega$. The perturbation is chosen to break the degeneracies in the spectrum of $\hat{H}_\ell$, since the r value is not well defined when there are a large number of degeneracies. This particular form of the perturbation also preserves the integrability of the unconstrained model, as well as the symmetries of $\hat{H}_\ell$.]

value $m_x \in \{-j, -j + 1, \ldots, j\}$) and $\hat{J}^2 \equiv (\hat{J}^x)^2 + (\hat{J}^y)^2 + (\hat{J}^z)^2$ [with eigenvalue $j(j + 1)$], are also valid eigenstates of the unconstrained Hamiltonian.

The right column of Fig. 2 also shows the density of states for the constrained Hamiltonian $\hat{H}_\ell$ with $\ell \in \{2, 3, \ldots, 6\}$ in the zero-momentum (assuming PBC), even-reflection symmetry sector. For $\ell \in \{2, 3\}$ [Figs. 2(i) and 2(k)] the density of states is approximately a smooth Gaussian [23]. As the constraint is weakened to $\ell \geqslant 4$, however, we begin to see deviation from the smooth density of states. This is due to the appearance of sharp peaks in the middle of the spectrum at integer or half integer multiples of Ω [see Figs. 2(e), (c), and (g)]. We find numerically that each of these peaks is degenerate with the number of degenerate states increasing exponentially in the chain length L (see Fig. 4). This is reminiscent of the degeneracies in the unconstrained model, which are also exponentially growing in system size (see the purple markers in Fig. 4). For the unconstrained model the degeneracies are associated with the conserved magnetization $\hat{J}^x$ and the
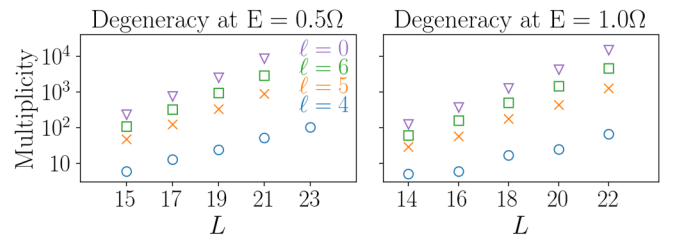

FIG. 4. For $\ell \geqslant 4$ and L even (odd) the degeneracy at integer (half integer) multiples of Ω increases exponentially in L. This resembles the degeneracy of the unconstrained model (the purple triangular markers). [Plotted data are restricted to the even-reflection and zero-momentum symmetry sector (PBC are assumed).]

associated quantum number m_x. However, for any nonzero ℓ this symmetry is broken and the degeneracies at integer/half integer multiples of Ω are not associated with any obvious local conserved quantities. In the next section we will show that the highly degenerate states in the spectrum of $\hat{H}_{\ell \geqslant 4}$ are in fact many-body scar states.

D. Extreme quantum scarring

Let $|E_\alpha\rangle$ and E_α be the eigenstates and eigenvalues of $\hat{H}_\ell$. For an observable $\hat{O}$ and a microcanonical energy window $\Lambda_E \equiv [E - \Delta E, E + \Delta E]$, we define the microcanonical average as $\overline{\mathcal{O}}_{\Lambda_E} \equiv \mathcal{N}_{\Lambda_E}^{-1} \sum_{E_\alpha \in \Lambda_E} \mathcal{O}_{\alpha\alpha}$, where $\mathcal{O}_{\alpha\alpha} = \langle E_\alpha | \hat{O} | E_\alpha \rangle$ are the EEVs of the observable and $\mathcal{N}_{\Lambda_E}$ is the number of states in Λ_E. With this definition one can formulate a strong and a weak version of the ETH.

For strong-ETH the condition $\mathcal{O}_{\alpha\alpha} \approx \overline{\mathcal{O}}_{\Lambda_E}$ must be satisfied by *all* EEVs in the energy window [37]. More precisely, the strong-ETH is satisfied if the quantity

$$I_s = \max_{E_\alpha \in \Lambda_E} \left| \mathcal{O}_{\alpha\alpha} - \overline{\mathcal{O}}_{\Lambda_E} \right| \qquad (5)$$

vanishes in the thermodynamic limit.

For weak-ETH it is enough that *most* eigenstates in the energy window satisfy $\mathcal{O}_{\alpha\alpha} \approx \overline{\mathcal{O}}_{\Lambda_E}$ [38]. In other words, the mean fluctuation around the microcanonical average

$$I_w = \left[\mathcal{N}_{\Lambda_E}^{-1} \sum_{E_\alpha \in \Lambda_E} \left(\mathcal{O}_{\alpha\alpha} - \overline{\mathcal{O}}_{\Lambda_E} \right)^2 \right]^{1/2} \qquad (6)$$

should vanish in the thermodynamic limit.

There is now considerable numerical evidence suggesting that the weak-ETH holds for generic integrable and nonintegrable quantum systems [38]: For generic integrable systems, I_w has a power-law decay with system size L [2,39,40], while for nonintegrable systems there are several finite-L numerical studies indicating that I_w decays exponentially with system size L [41–43] (although it has also been argued that the decay eventually becomes a power law as the system size increases [44]).

In the left column of Fig. 5 we plot the EEVs for the observable $\hat{J}^z = \frac{1}{2} \sum_i \hat{\sigma}_i^z$ in the zero-momentum symmetry sector of $\hat{H}_\ell$ (again we have assumed PBC). To calculate the ETH indicators I_w and I_s for this observable we choose a microcanonical energy window $\Lambda_E = [E - \Delta E, E + \Delta E]$ that is near the middle of the spectrum (shown in the gray shaded regions in the left column of Fig. 5). The center of the energy window is chosen at $E = 1.0\Omega$ ($E = 1.5\Omega$) if L is even (odd), anticipating that there are "special" eigenstates in the degenerate peaks located at those energies for $\ell \geqslant 4$. The width $\Delta E = 0.5\Omega$ is chosen to ensure that many states between degenerate peaks are also captured in the microcanonical energy window.

We see that the EEVs are, for the most part, concentrated around the microcanonical average (marked by a black x in the left column of Fig. 5). However, there are some eigenstates in Λ_E for which the EEV deviates significantly from the microcanonical average, giving a relatively large value of the strong-ETH indicator I_s. In the right column of Fig. 5 the blue lines show that I_s does not decay as the system size increases, verifying that the strong-ETH is indeed violated for these
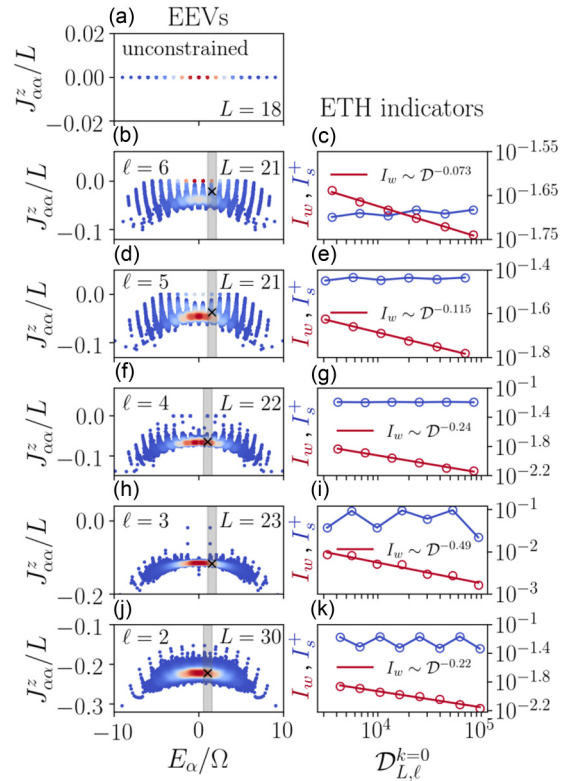

FIG. 5. The left column shows EEVs of the observable $\hat{O} = \hat{J}^z / L$ for the unconstrained model and also for constraint radius $\ell = 6, 5, 4, 3, 2$ (from top to bottom). The color scale indicates the density of data points. The right column shows the ETH indicators I_w (red) and I_s^+ (blue) plotted against the dimension $\mathcal{D}_{L,\ell}^{k=0}$ of the zero-momentum ($k = 0$) symmetry sector. [Note that we have plotted $I_s^+ = \max_{\Lambda_E}(\mathcal{O}_{\alpha\alpha} - \overline{\mathcal{O}}_{\Lambda_E})$ instead of $I_s = \max_{\Lambda_E} |\mathcal{O}_{\alpha\alpha} - \overline{\mathcal{O}}_{\Lambda_E}|$ since this gives cleaner results and is still a valid indicator of strong-ETH violation.] We see that the weak-ETH is satisfied for the constrained models (I_w decays as a power law in $\mathcal{D}$, i.e., exponentially in system size L), but the strong-ETH is violated (I_s^+ does not decay with system size).

eigenstates. The special eigenstates that prevent the decay of I_s are regarded as QMBS.

From Fig. 5(h), we notice that for $\ell = 3$ there are two scar eigenstates with a particularly pronounced violation of the strong-ETH. We find that, for any odd $L \geqslant 7$, these two scar states appear in the zero-momentum sector with *exactly* $E_\alpha = \pm\sqrt{7}/2$ and $J_{\alpha\alpha}^z = -3/7$ (up to numerical precision) [45]. We have also found numerically that these two special states are eigenstates of the total angular momentum operator $\hat{J}^2 = (\hat{J}^x)^2 + (\hat{J}^y)^2 + (\hat{J}^z)^2$ with the total angular momentum $j = 3/2$.

For $\ell \geqslant 4$ the scar states that are clearly visible in Figs. 5(b), 5(d), and 5(f) at $J_{\alpha\alpha}^z = 0$ are exactly the degenerate eigenstates that were discussed in the previous section with energies that are integer/half integer multiples of Ω for L even/odd. A closer examination of these degenerate integer/half integer energy eigenstates shows that they are Dicke states $|j, m_x\rangle$, with $m_x = E_\alpha/\Omega$ and $j \ll N/2$. In other words, they are eigenstates of the unconstrained Hamiltonian $\hat{H}_{\ell=0}$ as well as the constrained Hamiltonian $\hat{H}_{\ell \geqslant 4}$.
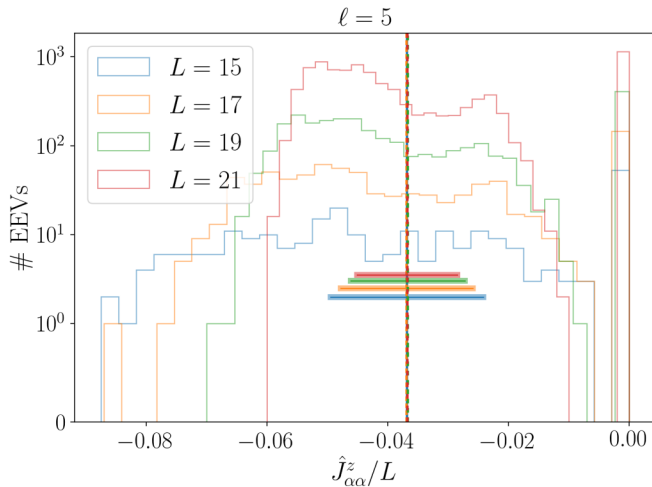
FIG. 6. The distribution of EEVs in the energy window Λ_E [the gray shaded region in Fig. 5(d)] for $\ell = 5$. The distribution is strongly skewed and has two main peaks, one at $J_{\alpha\alpha}^z/L \approx -0.05$ corresponding to the thermal eigenstates and one at $J_{\alpha\alpha}^z = 0$ for the many-body scars. The microcanonical average (the vertical dashed line) is located between the two peaks rather than at one of the peaks. However, as the system size increases, the fluctuations I_w (the error bars) decrease, indicating that the distribution is becoming more and more concentrated around the microcanonical average despite the large number of many-body scars.

This suggests that at $\ell = 4$ the constraint has been weakened sufficiently that some of the eigenstates of $\hat{H}_0$ can avoid the constraint completely. We note that $\langle j, m_x | \hat{J}^z | j, m_x \rangle = 0$ for Dicke states $|j, m_x\rangle$, which explains why $J_{\alpha\alpha}^z = 0$ for these scar states in Figs. 5(b), 5(d), and 5(f).

A clearly visible trend in the left column of Fig. 5 is that the scarring becomes more severe as $\ell \geqslant 3$ increases. It is natural to ask whether the scarring can become so extreme that not only is the strong-ETH violated but also the weak-ETH is violated. This might occur if, for example, there are always a similar number of Dicke scar states and thermal states in the energy window Λ_E, preventing the decay of the weak-ETH indicator I_w as the system size increases. This is illustrated in Fig. 6, where we show the distribution of EEVs in the energy window for $\ell = 5$. We see that the distribution is strongly skewed and has two main peaks, one corresponding to the thermal eigenstates and one for the many-body scars. The microcanonical average is located between the two peaks rather than at one of the peaks.

However, in the right column of Fig. 5, the red lines show that the weak indicator decays as $I_w \sim \mathcal{D}^{-\gamma}$ for $\ell \in \{2, 3, 4, 5, 6\}$, where $\mathcal{D}$ is the zero-momentum symmetry sector dimension. In Fig. 7 we plot the decay exponent γ as a function of ℓ. We see that for $\ell \geqslant 4$ the γ becomes smaller as ℓ increases and appears to be well approximated by the line $\gamma = 1/(a\ell + b)$ for real constants a and b. This trend suggests that the $I_w \sim \mathcal{D}^{-\gamma}$ scaling persists for finite ℓ, although the decay exponent can be very small for large ℓ. In other words, despite the skewed distribution of EEVs for large values of ℓ, most EEVs become concentrated around the microcanonical average as the system size increases.
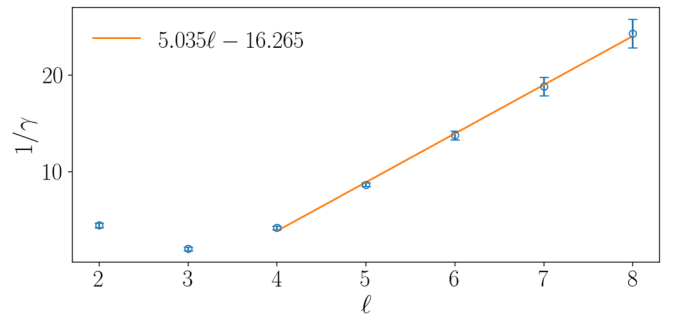

FIG. 7. As shown in the right column of Fig. 5, the weak ETH-indicator decays as $I_w \sim \mathcal{D}^{-\gamma}$. Here we plot the inverse of the decay exponent. We see here that for $4 \leqslant \ell \leqslant 8$ it closely fits the form $\gamma = 1/(a\ell + b)$, for constants a and b. Error bars are calculated from the error in fitting to the red markers in the right column of Fig. 5.

Finally, in Appendix C we repeat Figs. 5–7 but with a very different choice of the energy window Λ_E. We obtain similar results, showing that our results are not a relic of an unusual choice of the energy window Λ_E.

IV. CONCLUSION

In this paper we investigate the phenomenon of many-body scarring in quantum systems with dynamical constraints. We construct a class of spin-chain models for which the radius of a local dynamical constraint is given by a discrete variable ℓ. Increasing ℓ weakens the constraint by decreasing the dimension of the subspace that is excluded from the dynamics. We have shown that increasing ℓ also corresponds to more extreme quantum many-body scarring with the number of scar states increasing exponentially in system size for $\ell \geqslant 4$. Another example of a model exhibiting an exponentially increasing number of scars was given in Ref. [14]. However, our model differs in our ability to adjust the severity of scarring with our parameter ℓ.

To the best of our knowledge, our model $\hat{H}_\ell$ is the first that allows the degree of quantum scarring to be tuned. Since the scarring becomes more extreme with increasing ℓ it would be interesting to test our results for larger values and to explore the ultimate limit of extreme scarring. With our current numerical approach (exact diagonalization of dense matrices) this is challenging due to finite-size effects becoming more significant for larger values of ℓ. In the future larger system sizes may be accessed, however, by using the "shift-invert" algorithm with sparse matrices and focusing on a narrow energy window at finite density [42,46].

Note added. Recently we became aware that the same model is also studied in Ref. [47]. In that work, the focus is on the adjacency graph corresponding to $\hat{H}_\ell$ (and other constrained models), which is then used to provide interesting insights into the origin of many-body wave-function revivals in the dynamics.

ACKNOWLEDGMENTS

APPENDIX A: THE HAMILTONIAN FROM A STRONG ℓ-BODY INTERACTION

In this section we derive the effective Hamiltonian $\hat{H}_\ell$ [given in Eq. (1) of the main text] starting from a Hamiltonian of the form $\hat{H} = \hat{H}_0 + \varepsilon \sum_i \hat{\mathcal{P}}_i$ where $\hat{\mathcal{P}}_i = |\uparrow_i \uparrow_{i+1} \cdots \uparrow_{i+\ell-1}\rangle\langle\uparrow_i \uparrow_{i+1} \cdots \uparrow_{i+\ell-1}|$ is an ℓ-body interaction term. To begin, we transform to a rotating frame with respect to the unitary $\hat{R} = \exp\{it\varepsilon \sum_i \hat{\mathcal{P}}_i\}$. The Hamiltonian in the rotating frame is

$$\hat{H}_I = e^{it\varepsilon \sum_i \hat{\mathcal{P}}_i} \hat{H}_0 e^{-it\varepsilon \sum_i \hat{\mathcal{P}}_i}. \tag{A1}$$

Now, using the identity $e^{\pm it\varepsilon \hat{\mathcal{P}}_i} = \hat{\mathcal{Q}}_i + \hat{\mathcal{P}}_i e^{\pm it\varepsilon}$ where $\hat{\mathcal{Q}}_i = \hat{\mathbb{I}} - \hat{\mathcal{P}}_i$, we can rewrite the rotating frame Hamiltonian as

$$\hat{H}_I = \left[\prod_i (\hat{\mathcal{Q}}_i + \hat{\mathcal{P}}_i e^{it\varepsilon})\right] \hat{H}_0 \left[\prod_i (\hat{\mathcal{Q}}_i + \hat{\mathcal{P}}_i e^{-it\varepsilon})\right]. \tag{A2}$$

Expand the operator products as

$$\prod_i (\hat{\mathcal{Q}}_i + \hat{\mathcal{P}}_i e^{\pm it\varepsilon}) = \prod_i \hat{\mathcal{Q}}_i + e^{\pm it\varepsilon} \sum_j \hat{\mathcal{P}}_j \prod_{i, i\neq j} \hat{\mathcal{Q}}_i$$
$$+ e^{\pm i2t\varepsilon} \sum_{j_1 < j_2} \hat{\mathcal{P}}_{j_1} \hat{\mathcal{P}}_{j_2} \prod_{i, i\neq j_{1/2}} \hat{\mathcal{Q}}_i + \cdots$$
$$+ e^{irt\varepsilon} \sum_{j_1 < j_2 < \ldots < j_r} \hat{\mathcal{P}}_{j_1} \hat{\mathcal{P}}_{j_2} \ldots \hat{\mathcal{P}}_{j_r}$$
$$\times \prod_{i, i\neq j_i} \hat{\mathcal{Q}}_i + \cdots + \prod_i (e^{it\varepsilon} \hat{\mathcal{P}}_i)$$
$$= \sum_{r=0} e^{irt\varepsilon} \hat{\mathbb{P}}_r, \tag{A3}$$

where $\hat{\mathbb{P}}_r = \sum_{m_1 < m_2 < \ldots < m_r} \hat{\mathcal{P}}_{m_1} \hat{\mathcal{P}}_{m_2} \ldots \hat{\mathcal{P}}_{m_r} \prod_{n, n\neq m_i} \hat{\mathcal{Q}}_i$ is the projector onto the $\sum_i \hat{\mathcal{P}}_i = r$ eigenspace of the operator $\sum_i \hat{\mathcal{P}}_i$. This gives

$$\hat{H}_I = \sum_{r,r'} e^{i(r-r')t\varepsilon} \hat{\mathbb{P}}_r \hat{H}_0 \hat{\mathbb{P}}_{r'}. \tag{A4}$$

Assuming that ε is very large, the terms with $r \neq r'$ can be neglected by a rotating wave approximation

$$\hat{H}_I \approx \sum_r \hat{\mathbb{P}}_r \hat{H}_0 \hat{\mathbb{P}}_r = \sum_r \hat{H}_I^{(r)}, \tag{A5}$$

where $\hat{H}_I^{(r)} = \hat{\mathbb{P}}_r \hat{H}_0 \hat{\mathbb{P}}_r$. We see that the dynamics in the Hilbert space are fragmented into sectors that are labeled the (integer) eigenvalues of $\sum_i \hat{\mathcal{P}}_i$. That is, the effective Hamiltonian $\hat{H}_I^{(r)}$ describes the dynamics in the sector $\sum_i \hat{\mathcal{P}}_i = r$ and the state cannot evolve between sectors.

If we focus on the $r = 0$ sector, we see that the projector,

$$\mathbb{P}_{r=0} = \prod_i \hat{\mathcal{Q}}_i$$
$$= \prod_i (\hat{\mathbb{I}} - |\uparrow_i \uparrow_{i+1} \cdots \uparrow_{i+\ell-1}\rangle\langle\uparrow_i\uparrow_{i+1} \cdots \uparrow_{i+\ell-1}|), \tag{A6}$$

is exactly the projector $\hat{P}_\ell$ defined in Eq. (2) of the main text, and the $r = 0$ Hamiltonian $\hat{H}_I^{(r=0)} = \mathbb{P}_{r=0} \hat{H}_0 \mathbb{P}_{r=0}$ is exactly our effective Hamiltonian $\hat{H}_\ell$.

The ℓ-body interactions in the underlying Hamiltonian $\hat{H}$ may be considered unphysical for $\ell > 2$. However, our ℓ-body interaction between spin-1/2 particles can be mapped onto two-body nearest-neighbor interactions between higher spin particles. To see this, we can group the spin-1/2 particles in our chain into blocks of $\ell - 1$ contiguous spins (assuming that the chain length L is divisible by $\ell - 1$). Each block of the $\ell - 1$ spin-1/2 can then be mapped to a single spin-s particle, where $s = (2^{\ell-1} - 1)/2$. The interaction term $\hat{\mathcal{P}}_i = |\uparrow_i \uparrow_{i+1} \cdots \uparrow_{i+\ell-1}\rangle\langle\uparrow_i\uparrow_{i+1} \cdots \uparrow_{i+\ell-1}|$ in the Hamiltonian, after the same mapping, is then a two-body interaction between nearest-neighbor spin-s particles. This shows that our model Hamiltonian is not unphysical and can, in principle, be implemented in higher-spin systems, even for $\ell > 2$.

APPENDIX B: CONSTRAINED STATE SPACE DIMENSION

In this Appendix we derive the constrained Hilbert space dimension $\mathcal{D}_{L,\ell}^{\text{OBC}}$ for OBCs in Eq. (3) and $\mathcal{D}_{L,\ell}^{\text{PBC}}$ for PBCs in Eq. (4). We do this by considering basis states that are products of the $|\uparrow\rangle$ and $|\downarrow\rangle$ single-spin basis states, e.g., $|\uparrow \downarrow\downarrow\uparrow \ldots\rangle$. Only those basis states that do not have sequences of ℓ neighboring $\uparrow$ spins will contribute to the constrained Hilbert space dimension.

The case $L \leqslant \ell$. First, we observe that if $L < \ell$ the Hilbert space is not constrained since the constraint only takes effect if there are ℓ consecutive $\uparrow$ states. This gives $\mathcal{D}_{L,\ell}^{\text{OBC}} = \mathcal{D}_{L,\ell}^{\text{PBC}} = 2^L$ if $L < \ell$. If $L = \ell$ there is only one state $|\uparrow\rangle^{\otimes L}$ excluded from the constrained Hilbert space so that $\mathcal{D}_{L,L}^{\text{OBC}} = \mathcal{D}_{L,L}^{\text{PBC}} = 2^L - 1$.

OBCs. To derive the recurrence relation for $\mathcal{D}_{L,\ell}^{\text{OBC}}$ we begin with an open chain of length $L - 1 \geqslant \ell$ with the dimension $\mathcal{D}_{L-1,\ell}^{\text{OBC}}$. Adding a particle at the end of the chain (new site index $j = L$) gives a new open chain of length L. Any of the $\mathcal{D}_{L-1,\ell}^{\text{OBC}}$ basis states of the shorter chain are allowed if the new particle is added in the state $|\downarrow_L\rangle$. If the new particle is in the state $|\uparrow_L\rangle$, however, not all $\mathcal{D}_{L-1,\ell}^{\text{OBC}}$ basis states of the shorter chain are permitted because some will be excluded due to the constraint. In that case, if the $j = L - 1$ particle is in the state $|\downarrow_{L-1}\rangle$ then the $\mathcal{D}_{L-2,\ell}^{\text{OBC}}$ states of the remaining length $L - 2$ chain are allowed basis states. Alternatively, the $j = L - 1$ particle is in the state $|\uparrow_{L-1}\rangle$. In that case, if *its* neighbor ($j = L - 2$) is in the state $|\downarrow_{L-2}\rangle$ then the $\mathcal{D}_{L-3,\ell}^{\text{OBC}}$ states of the remaining length $L - 3$ chain are allowed basis states. We repeat this argument, proceeding along the chain, until we arrive at the scenario where the $\ell - 1$ particles at the end of the chain are all in their $|\uparrow\rangle$ state. Then, if the next particle ($j = L - \ell + 1$) in the $|\downarrow\rangle$ state the $\mathcal{D}_{L-\ell,\ell}^{\text{OBC}}$ states of the remaining chain are allowed. All other states basis states

are excluded by the constraint. We may visualize this counting more clearly as follows:

$$|\ldots\ldots\ldots\ldots\downarrow_L\rangle \quad : \quad \#\text{basis states} = \mathcal{D}^{\text{OBC}}_{L-1,\ell}$$

$$|\ldots\ldots\downarrow_{L-1}\uparrow_L\rangle \quad : \quad \#\text{basis states} = \mathcal{D}^{\text{OBC}}_{L-2,\ell}$$

$$|\ldots\downarrow_{L-2}\uparrow_{L-1}\uparrow_L\rangle \quad : \quad \#\text{basis states} = \mathcal{D}^{\text{OBC}}_{L-3,\ell}$$

$$\vdots$$

$$\vdots$$

$$|\ldots\downarrow_{L-\ell+1}\uparrow^{\otimes(\ell-1)}\rangle \quad : \quad \#\text{basis states} = \mathcal{D}^{\text{OBC}}_{L-\ell,\ell}$$

$$|\ldots\ldots\ldots\downarrow_{L-\ell}\uparrow^{\otimes\ell}\rangle \quad : \quad \#\text{basis states} = 0.$$

Adding all of these possibilities together gives the recurrence relation

$$\mathcal{D}^{\text{OBC}}_{L,\ell} = \mathcal{D}^{\text{OBC}}_{L-1,\ell} + \mathcal{D}^{\text{OBC}}_{L-2,\ell} + \mathcal{D}^{\text{OBC}}_{L-3,\ell} + \ldots + \mathcal{D}^{\text{OBC}}_{L-\ell,\ell}, \quad \text{(B1)}$$

with the initial conditions,

$$\mathcal{D}^{\text{OBC}}_{L,\ell} = 2^L, \quad \text{if} \quad L < \ell, \quad \text{(B2)}$$

$$\mathcal{D}^{\text{OBC}}_{L,\ell} = 2^L - 1, \quad \text{if} \quad L = \ell, \quad \text{(B3)}$$

as given in Eq. (3).

PBC. For periodic boundary conditions the counting is a little trickier. Suppose that we start with an open chain of length $L-1$ and the constrained space dimension $\mathcal{D}^{\text{OBC}}_{L-1,\ell}$. We would like to add a particle to the end of the chain (new site index $j = L$), giving a length L chain, and then bring the ends of the chain together to give PBC. Suppose that the new particle in added in the state $|\downarrow\rangle$. Then all $\mathcal{D}^{\text{OBC}}_{L-1,\ell}$ states of the shorter $L-1$ open chain contribute to the allowed basis states in the new chain with PBC. However, if we add the new particle in the $|\uparrow\rangle$ state there are a few possibilities, which we consider one-by-one. First, in the new PBC chain, we have the possibility that both neighbors of the added particle (i.e., the particles at $j = 1$ and at $j = L-1$) are in the $|\downarrow\rangle$ state giving the sequence $|\downarrow_1\ldots\downarrow_{L-1}\uparrow_L\rangle$. Then any state of the remaining length $L-3$ open chain is permitted, contributing $\mathcal{D}^{\text{OBC}}_{L-3,\ell}$ states to the count. Next, we could have either $|\downarrow_1\ldots\downarrow_{L-2}\uparrow_{L-1}\uparrow_L\rangle$ or $|\uparrow_1\downarrow_2\ldots\downarrow_{L-1}\uparrow_L\rangle$ with, in each case, the remaining length $L-4$ open chain contributing $\mathcal{D}^{\text{OBC}}_{L-4,\ell}$ states. Next, we could have $|\downarrow_1\ldots\downarrow_{L-3}\uparrow_{L-2}\uparrow_{L-1}\uparrow_L\rangle$, $|\uparrow_1\downarrow_2\ldots\downarrow_{L-2}\uparrow_{L-1}\uparrow_L\rangle$ or $|\uparrow_1\uparrow_2\downarrow_3\ldots\downarrow_{L-1}\uparrow_L\rangle$ with, in each case, the remaining length $L-5$ open chain contributing $\mathcal{D}^{\text{OBC}}_{L-5,\ell}$ states. We proceed step-by-step in this manner until, finally, we arrive at a sequence of $\ell+1$ spins of the form $\ldots\downarrow\underbrace{\uparrow\ldots\uparrow}_{\ell-1}\downarrow\ldots$, where one of the $\ell-1$ $\uparrow$'s must be in the $j = L$ position. This leads to $\ell-1$ possibilities for the location of such a sequence, with each contributing $\mathcal{D}^{\text{OBC}}_{L-\ell-1,\ell}$ states to the basis count. The count terminates at this point since the next step would lead to a configuration with ℓ contiguous $\uparrow$ spins, which is forbidden by the constraint. We may visualize the counting more clearly as follows:

$$|\ldots\downarrow_L\ldots\rangle \quad : \quad \#\text{basis states} = \mathcal{D}^{\text{OBC}}_{L-1,\ell}$$

$$|\ldots\downarrow_{L-1}\uparrow_L\downarrow_1\ldots\rangle \quad : \quad \#\text{basis states} = \mathcal{D}^{\text{OBC}}_{L-3,\ell}$$

$$|\ldots\downarrow\uparrow\uparrow\downarrow\ldots\rangle \quad : \quad \#\text{basis states} = \mathcal{D}^{\text{OBC}}_{L-4,\ell} \times 2$$
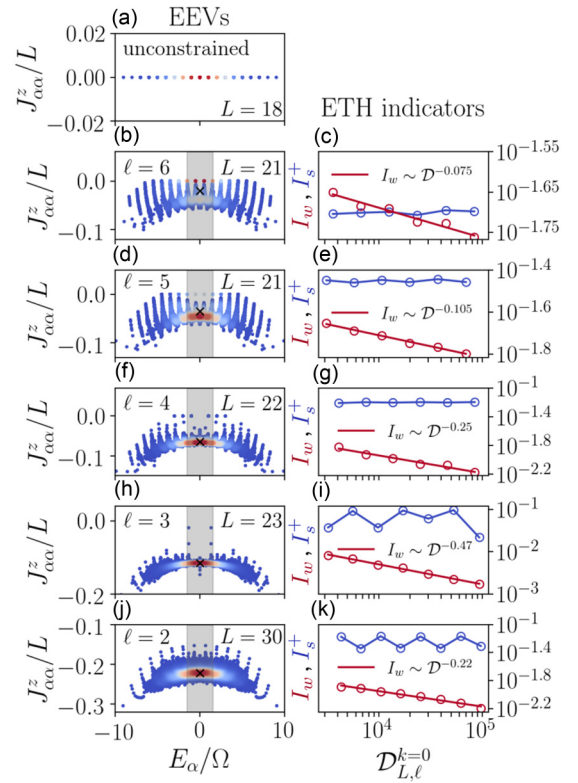

FIG. 8. We repeat Fig. 5 in the main text, but with a very different choice of energy window: $\Lambda_E = [E - \Delta E, E + \Delta E]$ with $E = 0$ and $\Delta E = 1.5\Omega$, the gray shaded region. The results in the right column are essentially unchanged compared with Fig. 5 in the main text.

$$|\ldots\downarrow\uparrow\uparrow\uparrow\downarrow\ldots\rangle \quad : \quad \#\text{basis states} = \mathcal{D}^{\text{OBC}}_{L-5,\ell} \times 3$$

$$\vdots$$

$$\vdots$$

$$|\ldots\downarrow\uparrow^{\otimes(\ell-1)}\downarrow\ldots\rangle \quad : \quad \#\text{basis states} = \mathcal{D}^{\text{OBC}}_{L-\ell-1,\ell} \times (\ell-1)$$

$$|\ldots\downarrow\uparrow^{\otimes\ell}\downarrow\ldots\rangle \quad : \quad \#\text{basis states} = 0.$$
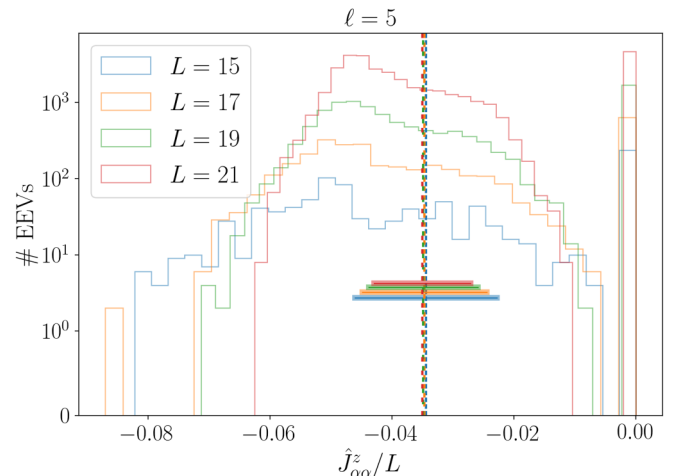

FIG. 9. We repeat Fig. 6 but with the energy window shown in the gray shaded region of Fig. 8(d).
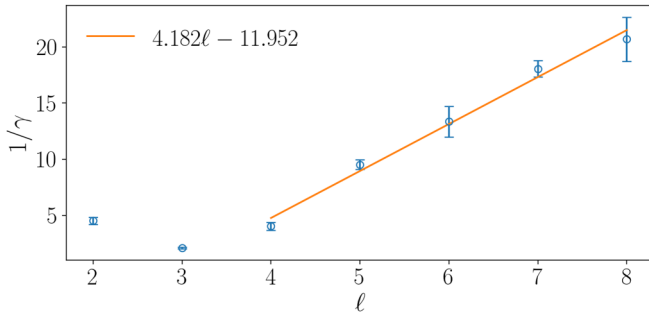
FIG. 10. In the new energy window the the decay exponents for I_w follow similar behavior as in Fig. 7.

Adding all of these possibilities together finally gives the periodic chain recurrence relation

$$\mathcal{D}_{L,\ell}^{\mathrm{PBC}} = \mathcal{D}_{L-1,\ell}^{\mathrm{OBC}} + \mathcal{D}_{L-3,\ell}^{\mathrm{OBC}} + 2\mathcal{D}_{L-4,\ell}^{\mathrm{OBC}} + 3\mathcal{D}_{L-5,\ell}^{\mathrm{OBC}} \cdots$$
$$+ (\ell - 1)\mathcal{D}_{L-\ell-1,\ell}^{\mathrm{OBC}}. \tag{B4}$$

APPENDIX C: FIGS. 5–7 ARE REPEATED FOR A DIFFERENT CHOICE OF ENERGY WINDOW Λ_E

In Figs. 8–10 we show that our results in Figs. 5–7 are not significantly changed if we choose a very different energy window Λ_E.

[1] L. D'Alessio, Y. Kafri, A. Polkovnikov, and M. Rigol, From quantum chaos and eigenstate thermalization to statistical mechanics and thermodynamics, Adv. Phys. **65**, 239 (2016).

[2] G. Biroli, C. Kollath, and A. M. Läuchli, Effect of Rare Fluctuations on the Thermalization of Isolated Quantum Systems, Phys. Rev. Lett. **105**, 250401 (2010).

[3] I. V. Gornyi, A. D. Mirlin, and D. G. Polyakov, Interacting Electrons in Disordered Wires: Anderson Localization and Low-t Transport, Phys. Rev. Lett. **95**, 206603 (2005).

[4] D. M. Basko, I. L. Aleiner, and B. L. Altshuler, Metal–insulator transition in a weakly interacting many-electron system with localized single-particle states, Ann. Phys. **321**, 1126 (2006).

[5] A. Pal and D. A. Huse, Many-body localization phase transition, Phys. Rev. B **82**, 174411 (2010).

[6] D. Abanin, W. De Roeck, W. W. Ho, and F. Huveneers, A rigorous theory of many-body prethermalization for periodically driven and closed quantum systems, Commun. Math. Phys. **354**, 809 (2017).

[7] D. V. Else, P. Fendley, J. Kemp, and C. Nayak, Prethermal Strong Zero Modes and Topological Qubits, Phys. Rev. X **7**, 041062 (2017).

[8] S. Nulty, J. Vala, D. Meidan, and G. Kells, Constrained thermalization and topological superconductivity, Phys. Rev. B **102**, 054508 (2020).

[9] G. Kells, Multiparticle content of majorana zero modes in the interacting p-wave wire, Phys. Rev. B **92**, 155434 (2015).

[10] P. Fendley, Strong zero modes and eigenstate phase transitions in the XYZ/interacting majorana chain, J. Phys. A: Math. Theor. **49**, 30LT01 (2016).

[11] N. Moran, D. Pellegrino, J. K. Slingerland, and G. Kells, Parafermionic clock models and quantum resonance, Phys. Rev. B **95**, 235127 (2017).

[12] Z. Lan, M. van Horssen, S. Powell, and J. P. Garrahan, Quantum Slow Relaxation and Metastability Due to Dynamical Constraints, Phys. Rev. Lett. **121**, 040603 (2018).

[13] N. Pancotti, G. Giudice, J. I. Cirac, J. P. Garrahan, and M. C. Bañuls, Quantum East Model: Localization, Nonthermal Eigenstates, and Slow Dynamics, Phys. Rev. X **10**, 021051 (2020).

[14] N. Shiraishi and T. Mori, Systematic Construction of Counterexamples to the Eigenstate Thermalization Hypothesis, Phys. Rev. Lett. **119**, 030601 (2017).

[15] S. Moudgalya, S. Rachel, B. A. Bernevig, and N. Regnault, Exact excited states of nonintegrable models, Phys. Rev. B **98**, 235155 (2018).

[16] S. Moudgalya, N. Regnault, and B. A. Bernevig, Entanglement of exact excited states of affleck-kennedy-lieb-tasaki models: Exact results, many-body scars, and violation of the strong eigenstate thermalization hypothesis, Phys. Rev. B **98**, 235156 (2018).

[17] V. Khemani, C. R. Laumann, and A. Chandran, Signatures of integrability in the dynamics of Rydberg-blockaded chains, Phys. Rev. B **99**, 161101(R) (2019).

[18] W. W. Ho, S. Choi, H. Pichler, and M. D. Lukin, Periodic Orbits, Entanglement, and Quantum Many-Body Scars in Constrained Models: Matrix Product State Approach, Phys. Rev. Lett. **122**, 040603 (2019).

[19] N. Shibata, N. Yoshioka, and H. Katsura, Onsager's Scars in Disordered Spin Chains, Phys. Rev. Lett. **124**, 180604 (2020).

[20] P. A. McClarty, M. Haque, A. Sen, and J. Richter, Disorder-free localization and many-body quantum scars from magnetic frustration, Phys. Rev. B **102**, 224303 (2020).

[21] J. Richter and A. Pal, Anomalous hydrodynamics in a class of scarred frustration-free hamiltonians, Phys. Rev. Research **4**, L012003 (2022).

[22] J. Jeyaretnam, J. Richter, and A. Pal, Quantum scars and bulk coherence in a symmetry-protected topological phase, Phys. Rev. B **104**, 014424 (2021).

[23] C. J. Turner, A. A. Michailidis, D. A. Abanin, M. Serbyn, and Z. Papić, Weak ergodicity breaking from quantum many-body scars, Nat. Phys. **14**, 745 (2018).

[24] C. J. Turner, A. A. Michailidis, D. A. Abanin, M. Serbyn, and Z. Papić, Quantum scarred eigenstates in a Rydberg atom chain: Entanglement, breakdown of thermalization, and stability to perturbations, Phys. Rev. B **98**, 155134 (2018).

[25] N. Shiraishi, Connection between quantum-many-body scars and the affleck–kennedy–lieb–tasaki model from the viewpoint of embedded Hamiltonians, J. Stat. Mech. (2019) 083103.

[26] C.-J. Lin and O. I. Motrunich, Exact Quantum Many-Body Scar States in the Rydberg-Blockaded Atom Chain, Phys. Rev. Lett. **122**, 173401 (2019).

[27] S. Choi, C. J. Turner, H. Pichler, W. W. Ho, A. A. Michailidis, Z. Papić, M. Serbyn, M. D. Lukin, and D. A. Abanin, Emergent SU(2) Dynamics and Perfect Quantum Many-Body Scars, Phys. Rev. Lett. **122**, 220603 (2019).

[28] V. Khemani, M. Hermele, and R. Nandkishore, Localization from Hilbert space shattering: From theory to physical realizations, Phys. Rev. B **101**, 174204 (2020).

[29] S. Dooley and G. Kells, Enhancing the effect of quantum many-body scars on dynamics by minimizing the effective dimension, Phys. Rev. B **102**, 195114 (2020).

[30] S. Dooley, Robust quantum sensing in strongly interacting systems with many-body scars, PRX Quantum **2**, 020330 (2021).

[31] H. Bernien, S. Schwartz, A. Keesling, H. Levine, A. Omran, H. Pichler, S. Choi, A. S. Zibrov, M. Endres, M. Greiner, V. Vuletić, and M. D. Lukin, Probing many-body dynamics on a 51-atom quantum simulator, Nature (London) **551**, 579 (2017).

[32] I. Lesanovsky, Many-Body Spin Interactions and the Ground State of a Dense Rydberg Lattice Gas, Phys. Rev. Lett. **106**, 025301 (2011).

[33] G. Barontini, L. Hohmann, F. Haas, J. Estève, and J. Reichel, Deterministic generation of multiparticle entanglement by quantum Zeno dynamics, Science **349**, 1317 (2015).

[34] I. Lesanovsky and H. Katsura, Interacting Fibonacci anyons in a Rydberg gas, Phys. Rev. A **86**, 041601(R) (2012).

[35] M. Gardner, *The 2nd Scientific American Book of Mathematical Puzzles and Diversions* (The University of Chicago Press, Chicago, 1987).

[36] V. Oganesyan and D. A. Huse, Localization of interacting fermions at high temperature, Phys. Rev. B **75**, 155111 (2007).

[37] H. Kim, T. N. Ikeda, and D. A. Huse, Testing whether all eigenstates obey the eigenstate thermalization hypothesis, Phys. Rev. E **90**, 052105 (2014).

[38] T. Mori, T. N. Ikeda, E. Kaminishi, and M. Ueda, Thermalization and prethermalization in isolated quantum systems: A theoretical overview, J. Phys. B: At. Mol. Opt. Phys. **51**, 112001 (2018).

[39] T. N. Ikeda, Y. Watanabe, and M. Ueda, Finite-size scaling analysis of the eigenstate thermalization hypothesis in a one-dimensional interacting Bose gas, Phys. Rev. E **87**, 012125 (2013).

[40] V. Alba, Eigenstate thermalization hypothesis and integrability in quantum spin chains, Phys. Rev. B **91**, 155123 (2015).

[41] R. Steinigeweg, A. Khodja, H. Niemeyer, C. Gogolin, and J. Gemmer, Pushing the Limits of the Eigenstate Thermalization Hypothesis Towards Mesoscopic Quantum Systems, Phys. Rev. Lett. **112**, 130403 (2014).

[42] W. Beugeling, R. Moessner, and M. Haque, Finite-size scaling of eigenstate thermalization, Phys. Rev. E **89**, 042112 (2014).

[43] T. N. Ikeda and M. Ueda, How accurately can the microcanonical ensemble describe small isolated quantum systems? Phys. Rev. E **92**, 020102(R) (2015).

[44] Y. Huang, Finite-size scaling analysis of eigenstate thermalization, Ann. Phys. **438** 168761 (2022).

[45] We note that for L odd, as we increase $L \to L + 2$ this special state alternates between the $(k, p) = (0, 1)$ and the $(k, p) = (0, -1)$ sectors, where k denotes momentum and p denotes reflection parity.

[46] D. J. Luitz, N. Laflorencie, and F. Alet, Many-body localization edge in the random-field heisenberg chain, Phys. Rev. B **91**, 081103(R) (2015).

[47] J.-Y. Desaules, K. Bull, A. Daniel, and Z. Papić, Hypergrid subgraphs and the origin of scarred quantum walks in the many-body Hilbert space, arXiv:2112.06885 [quant-ph].